COMMUNICATIONS MATERIALS

ARTICLE

https://doi.org/10.1038/s43246-020-00087-x OPEN

Extreme shear-deformation-induced modification of defect structures and hierarchical microstructure in an Al–Si alloy

Bharat Gwalani [1], Matthew Olszta[2], Soumya Varma[3,7], Lei Li [1], Ayoub Soulami[1], Elizabeth Kautz [4], Siddhartha Pathak[3,7], Aashish Rohatgi[2], Peter V. Sushko[1], Suveen Mathaudhu[2,5,6], Cynthia A. Powell[2] & Arun Devaraj [1✉]

Extreme shear deformation is used for several material processing methods and is unavoidable in many engineering applications in which two surfaces are in relative motion against each other while in physical contact. The mechanistic understanding of the microstructural evolution of multi-phase metallic alloys under extreme shear deformation is still in its infancy. Here, we highlight the influence of shear deformation on the microstructural hierarchy and mechanical properties of a binary as-cast Al-4 at.% Si alloy. Shear-deformation-induced grain refinement, multiscale fragmentation of the eutectic Si-lamellae, and metastable solute saturated phases with distinctive defect structures led to a two-fold increase in the flow stresses determined by micropillar compression testing. These results highlight that shear deformation can achieve non-equilibrium microstructures with enhanced mechanical properties in Al–Si alloys. The experimental and computational insights obtained here are especially crucial for developing predictive models for microstructural evolution of metals under extreme shear deformation.

[1] Physical and Computational Sciences Directorate, Pacific Northwest National Laboratory, Richland, WA 99352, USA. [2] Energy and Environment Directorate, Pacific Northwest National Laboratory, Richland, WA 99352, USA. [3] Chemical and Materials Engineering, University of Nevada, Reno, NV 89557, USA. [4] National Security Directorate, Pacific Northwest National Laboratory, Richland, WA 99352, USA. [5] Mechanical Engineering Department, University of California, Riverside, Riverside, CA 92521, USA. [6] Material Science and Engineering Program, University of California, Riverside, Riverside, CA 92521, USA. [7] Present address: Department of Materials Science and Engineering, Iowa State University, Ames, IA 50012, USA. ✉email: arun.devaraj@pnnl.gov

Solid-phase processing (SPP) methods, such as friction stir processing (FSP)[1] and shear-assisted processing and extrusion[2], employ extreme shear deformation to achieve highly refined microstructures with improved mechanical properties in structural materials[3–7]. Extreme shear deformation is also prevalent in the field of tribology and occurs due to friction between two surfaces that are in contact and in relative motion[8–10]. Recently, the atomic-scale mechanisms of microstructural evolution under shear deformation have been a topic of growing interest[11–16]. Specifically, it has been hypothesized that there is competition in immiscible binary alloys between opposing forces of shear-induced chemical intermixing and thermally activated diffusion[17]. This competition has been postulated to result in increased solubility of elements, thereby causing the formation of metastable supersaturated solutions, even in alloys with moderately positive enthalpies of mixing (such as Cu–Ag)[13,18]. An et al. detailed the interfacial changes and dislocation transfer across the severely shear deformed Ag–Cu interfaces[19]. Nanolayer formation through morphological self-organization has also been reported after shear deformation of highly immiscible alloys such as Cu–Nb[11,20]. However, when considering alloy systems with a ductile matrix and a brittle second phase precipitate that has limited solubility in each other, it is currently unknown how shear deformation will modify the microstructure. Open research questions include: (1) will the shear deformation lead to hierarchical fragmentation of the brittle phase and inward diffusion of the matrix element; (2) to what extent will grain refinement occur for the ductile matrix; and (3) can true solute supersaturation of the matrix phase be attained at an atomic scale? Additionally, there is very limited understanding of the impact of shear deformation on microstructural evolution and mechanical properties.

To address these knowledge gaps, we selected a binary Al-4 at.% Si alloy, which is a castable alloy widely used in the defense, aerospace, and automotive industries. This lightweight alloy offers high strength, corrosion resistance, good thermal conductivity, as well as a low coefficient of thermal expansion[21–23]. The coarse eutectic structures, massive Si particles, porosity, and uneven shrinkage typically exhibited in this alloy system can be major drawbacks when processed using conventional casting methods[24–27]. Mechanical properties can be improved in Al–Si alloys by producing a fine-scale distribution of Si particles and eliminating porosity. Heat treatments and chemical modifications have been used to refine the eutectic microstructure of Al–Si alloys[27–29]. Heat treatments at high temperatures for extended time durations can be used to spheroidize Si, but such treatments also coarsen the Si particles, degrading mechanical properties and increasing production costs[30,31]. Additions of sodium (Na), antimony (Sb), and strontium (Sr) are commonly made as eutectic modifiers that can spheroidize the otherwise coarse acicular Si particles, effectively improving the mechanical performance of the Al–Si alloys[1,32–35]. However, these effects can diminish in the case of Na at elevated temperatures, or result in an increased amount of gas pickup and porosity in the case of Sr and Sb[36–38]. Sb also poses environmental safety concerns[30] because of its health hazard and ability to cause severe poisoning. As solid-phase processing (SPP) techniques can result in refined microstructures and do not require the melting of the alloy, they can also be much less energy intensive than more conventional approaches. For example, the FSP of an Al–Si–Mg alloy was effective in uniformly distributing the acicular Si phase and completely healing casting porosities[5,36]. Nelaturu et al. demonstrated an improvement in fatigue life of an Al-7Si-0.3Mg (A356 alloy) by one order of magnitude after FSP. While the advantages of SPP approaches to Al–Si-based alloys have been demonstrated in past[5,36,39], a clear understanding of transformation pathways and mass redistribution during SPP is lacking. Therefore, in this work, a detailed analysis of the shear-deformation-induced microstructural refinement and mechanical property changes in a model as-cast Al-4 at.% Si alloy is conducted using an experimental and computational study.

Results and discussion

The as-cast and homogenized Al–4Si alloy consists of a dendritic microstructure with a hypoeutectic Al matrix and a eutectic Al–Si inter-dendritic region (Fig. 1a–c and Supplementary Figs. 1–4). The grain size of the as-cast Al–4Si alloy ranges from 300 to 600 μm. The APT proximity histogram between the eutectic Al and Si phases (Fig. 1d) revealed the average composition of Si dissolved in Al to be 1.26 ± 0.01 at.%, while there was no Al dissolved in the eutectic Si phase. The crystal structure was verified using TEM-selected area electron diffraction, as shown in Supplementary Fig. 2a–c; the Al rich phase had a face-centered cubic and the Si rich second phase had diamond cubic crystal structure. The APT analysis identified 0.10 ± 0.02 at.% Si in the hypoeutectic Al matrix measured from the center of the dendrite (see Supplementary Fig. 2d, e). Thus, based on these observations, Si concentration ranged from 0.10 at.% in the hypoeutectic Al to 1.26 at.% in the Al adjacent to the eutectic Si phase. The TEM results also highlighted coherent Al-rich nanoscale precipitates (5–10 nm in diameter) within the eutectic Si phase (Fig. 1e–g). These Al nanoprecipitates were accompanied by a void at their periphery (Fig. 1f, g). Refer to the Supplementary videos 1 and 2 and Supplementary Figs. 3 and 4 showing the distribution of nanoprecipitates and the voids. Barrirero et al. observed similar nanoprecipitates in Al–7 wt% Si (i.e., ~6.8 at.% Si) using TEM and APT and suggested that these precipitates can have variable compositions ranging from 10 to 50 at.% Al [33,40].

After characterizing the as-cast and homogenized alloy microstructure, we subjected the metallographically polished surface of the Al–4Si alloy to reciprocating shear deformation using a pin-on-disk tribometer (see schematic in Fig. 2a). The details of the tribometer test conditions are provided in "Methods" and Supplementary Fig. 5. After 5000 cycles of reciprocating shear deformation, the sample was cross-sectioned (see schematic in Fig. 2b), and the microstructure in the deformed region was analyzed using SEM-BSE imaging (Fig. 2c). The microstructure in the 30 μm thick shear-deformed region was substantially refined (Fig. 2c), and SEM Energy Dispersive Spectroscopy (EDS) mapping revealed fragmentation of Si precipitates in the shear-deformed region (Fig. 3d, low-magnification maps in Supplementary Fig. 6). The average Vickers hardness in the preprocessed region was measured to be 34 ± 05 Hv (28 Hv in center of dendrite and 37 Hv in the inter-dendritic eutectic region), while a hardness of 89 ± 11 Hv was measured in the post-deformation region (Supplementary Fig. 7). A nano indention hardness mapping was also performed which does not show conclusive trends as the alloy consists of a dual phase microstructure with very different hardness values of each phase and therefore the scatter in the hardness in the base material is very high, which makes it difficult to observe the trend in the hardness change due to deformation. A very high scatter was also observed by Stoyanov et al.[41]. Stoyanov et al. observed the change in nanomechanical properties of the shear deformed layer by tribometer as a function of contact pressure and observed that the lower pressure (15 MPa) showed a much higher degree of mechanical mixing and grain refinement compared to the higher pressure of 35 MPa in Al–Si alloy[41].

Micropillar testing under compression, shown in Fig. 2e, indicates that the 4% offset flow strength of the shear-deformed regions (0.33 ± 0.12 GPa) is two times higher than that of the as-cast Al matrix (0.14 ± 0.02 GPa) or the eutectic Al–Si regions

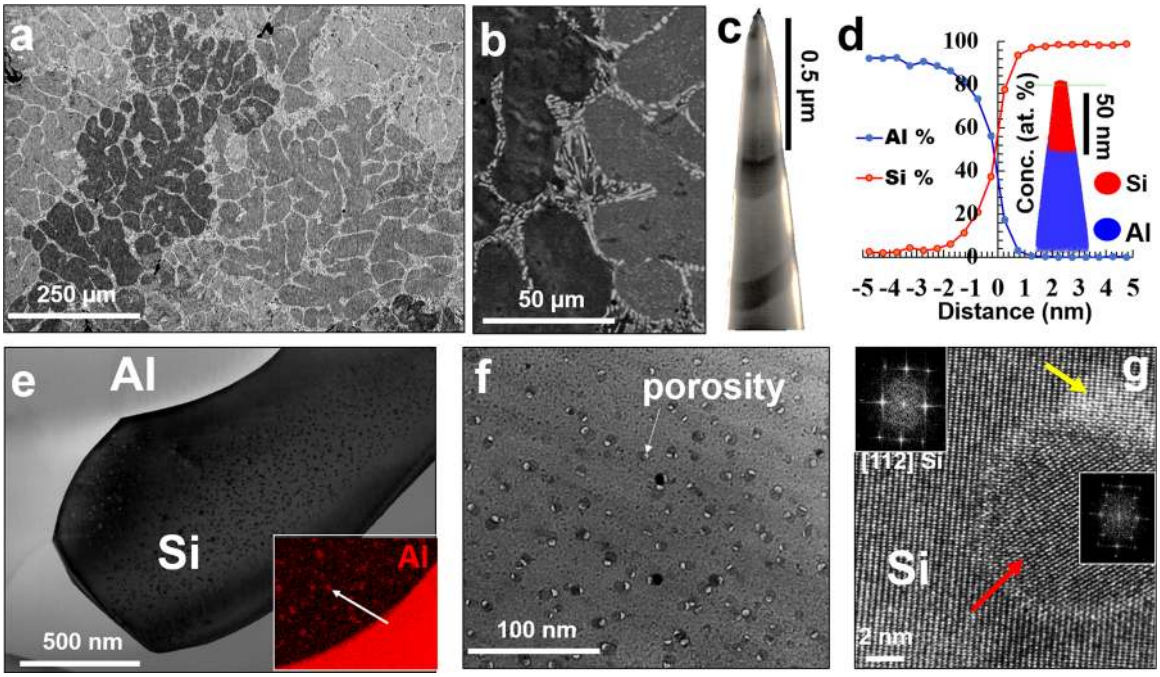

Fig. 1 Microstructure of as-cast Al–4Si alloy. a Low-magnification SEM-BSE image of the as-cast Al–4Si alloy, with dendritic grains (dark) separated by inter-dendritic regions (bright) consisting of eutectic Al–Si phases. **b** Higher-magnification SEM-BSE image of the eutectic region. **c** SEM image of a FIB-prepared APT needle sample from the eutectic region showing stripes corresponding to Si precipitates in the needle. **d** An APT reconstruction of the eutectic region with the Si (red) and Al (blue) distributions (inset) and compositional profiles across the Al and Si phases. **e** Bright-field TEM (BFTEM) image showing the acicular Si phase in the eutectic region. STEM-EDS Al map at the same magnification (inset) reveals the Al-rich nanoprecipitates inside the eutectic Si phase (white arrow). **f** Nanoscale voids adjacent to the Al-rich nanoprecipitates inside the eutectic Si phase as imaged using Fresnel contrast imaging. **g** An Al-rich particle inside the eutectic Si phase in a STEM (high angle annular dark field) HAADF image. Arrows point to an Al-rich nanoprecipitate (red) and nanovoid (yellow). The inset (top left) is the FFT of the image with Si phase aligned on [112] direction while on right is the FFT from the Al-rich nanoprecipitate.

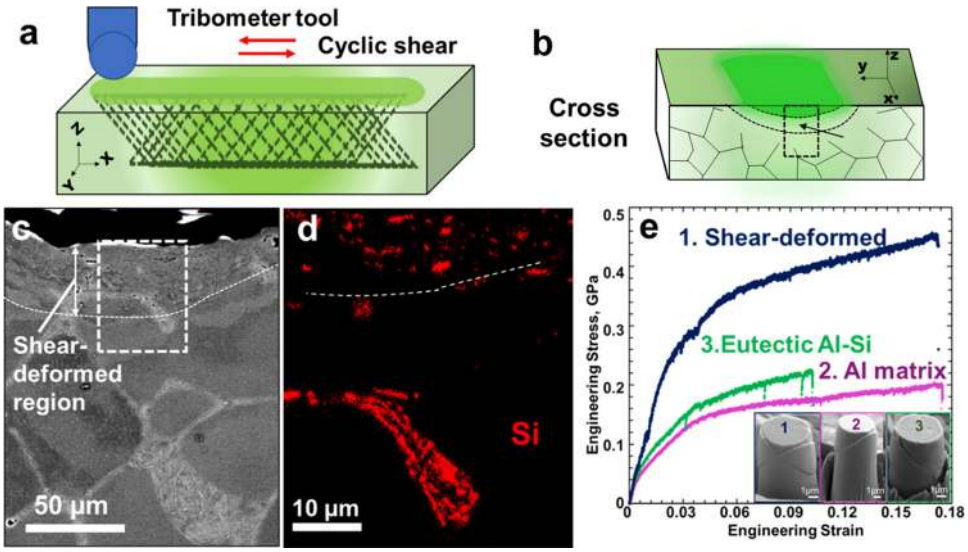

Fig. 2 Cyclic shear deformation of Al–4Si. a The procedure used to generate reciprocal shear deformation using a pin-on-disk tribometer. **b** Schematic of a shear-deformed microstructure cross-section, the box highlights the location of microstructural and mechanical property assessment. **c** SEM-BSE image with the dashed curve highlighting the boundary between the 30 µm thick shear-deformed region and the undeformed microstructure below. The dashed rectangle highlights the region shown in **d**. **d** EDS map of the Si distribution in the shear-deformed and adjacent undeformed regions. A dotted white line is used to delineate the sheared and unsheared region in both **c** and **d**. **e** Micropillar compression stress–strain curves for the shear-deformed region and undeformed eutectic Al–Si and Al matrix. Inset: secondary electron SEM images of deformed pillars of all three regions.

(0.18 ± 0.01 GPa). An increase of 0.19 GPa in 4% offset flow strength is observed in our experiments could be due to a combination of Hall–Petch strengthening, matrix supersaturation, and second phase strengthening by nanoprecipitation, and fragmentation of Si phase. The grain boundary strength of the Al matrix (~100 nm), calculated using the Hall–Petch relation with K_o for pure Al to be ~0.002 GPa. mm$^{1/2}$ and σ_o of ~0.01 GPa[42] is ~0.213 GPa. Hence, the extra 0.17 GPa observed experimentally is

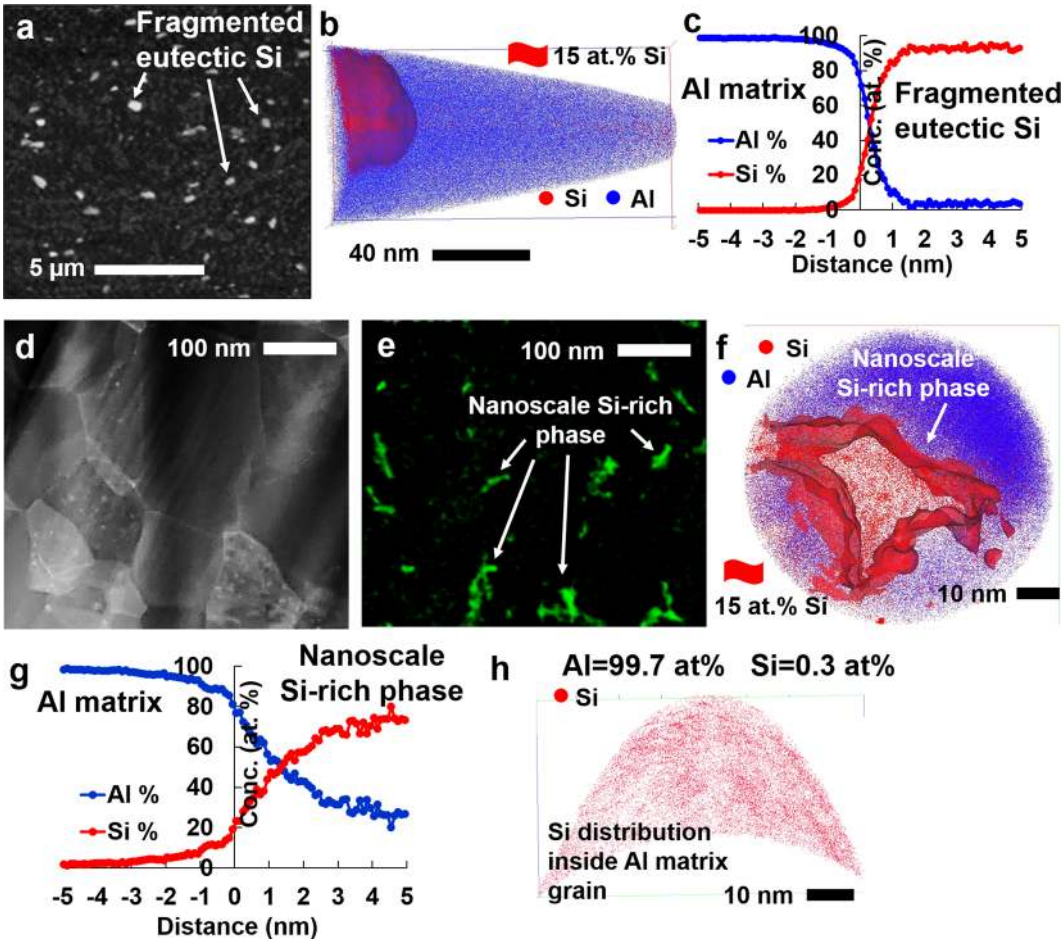

Fig. 3 Characterization of shear deformed Al–4Si alloy. Al–4–Si microstructure in the sheared region. **a** SEM-BSE image of the fragmented eutectic Si phase (bright contrast phase). **b**, **c** APT reconstruction of the interface, as well as the compositional change across it, between the fragmented eutectic Si phase and the Al matrix. **d** STEM-HAADF image of the Al matrix. **e** Si STEM-EDS map of the same region as in **d** showing the distribution of nanoscale, Si-rich phases at Al grain boundaries. **f** APT reconstruction of a nanoscale, Si-rich phase within the ultrafine-grained Al matrix. **g** The compositional change across the Al matrix and nanoscale Si-rich phase. **h** APT reconstruction of Si distribution in intragranular regions of the nanograined Al matrix.

likely due to matrix supersaturation and/or the refinement of the Si phase.

High-resolution characterization of the shear-deformed microstructure revealed three levels of microstructural hierarchy in terms of Si distribution. The first level of microstructural hierarchy is formed by the 500 nm to 1 µm fragmented eutectic Si phase, highlighted using white arrows in the high-magnification BSE image in Fig. 3a. The average composition of this phase was found to be 95.5 ± 1.5 at.% Si and 4.5% ± 0.5 at.% Al, as quantified using proximity histogram analysis across a 15 at.% Si iso-composition surface in the APT reconstruction (see Fig. 3b, c). Between these fragmented eutectic Si phases, ultrafine Al grains with an average grain size of 90 ± 35 nm were revealed using STEM imaging (Fig. 3d). As illustrated by the STEM-EDS map (Fig. 3e), these Al grains have a nanoscale, Si-rich phase at grain boundaries, that constitutes the second level of microstructural hierarchy. A proximity histogram across a 15 at.% Si iso-composition surface of APT-reconstructed regions (Fig. 3f, g) highlights that the composition of these Si-rich regions is 74.82 ± 1.8 at.% Si and 25.18 ± 0.7 at.% Al. In addition, the average composition of the grain interiors of the ultrafine-grained Al matrix in the shear-deformed region was measured to be 0.31 ± 0.01 at.% Si using APT. Si was distributed heterogeneously, forming nanoscale Si-rich clusters (Fig. 3h). These clusters constitute the third level of microstructural hierarchy. Shear-deformation-induced Si clustering in an Al matrix can modify the local stacking-fault energy and therefore potentially lead to the formation of stacking faults[39,43–45]. To verify this hypothesis, additional TEM analysis was conducted to analyze defect structures in the shear-deformed region.

The BFTEM image of the shear-deformed region shows the ultrafine-grained Al matrix and a fragmented eutectic Si phase (Fig. 4a). A high density of vacancy Frank loops was observed in the Al matrix (Fig. 4b). Similar Frank loops, 2–20 nm in size, were also observed by Wu et al. in pure Al after equal channel annular processing[46]. These Frank loops had stacking faults on the (111) planes, as highlighted in Fig. 4c. The phase contrast image in Fig. 4d shows the clear discontinuity in the (111) planes of Al, and the fast Fourier transformation inset of the phase contrast image depicts the [110] zone axis of the Al grain. In addition, we noticed a high density of microtwins in the fragmented eutectic Si phase along the {110} direction (Fig. 4e). The phase contrast image of the fragmented eutectic Si phase given in Fig. 4f also revealed a stacking fault that sheared an Al-rich nanoprecipitate, further confirming that these faults were formed during shear deformation. These stacking faults originated from the dissociation of 1/2⟨110⟩ type edge dislocations into two 1/6⟨112⟩ Shockley partial dislocations and are commonly observed in low-stacking-fault energy materials[47]. We note that the nanovoids associated with Al-rich nanoprecipitates in the eutectic Si phase

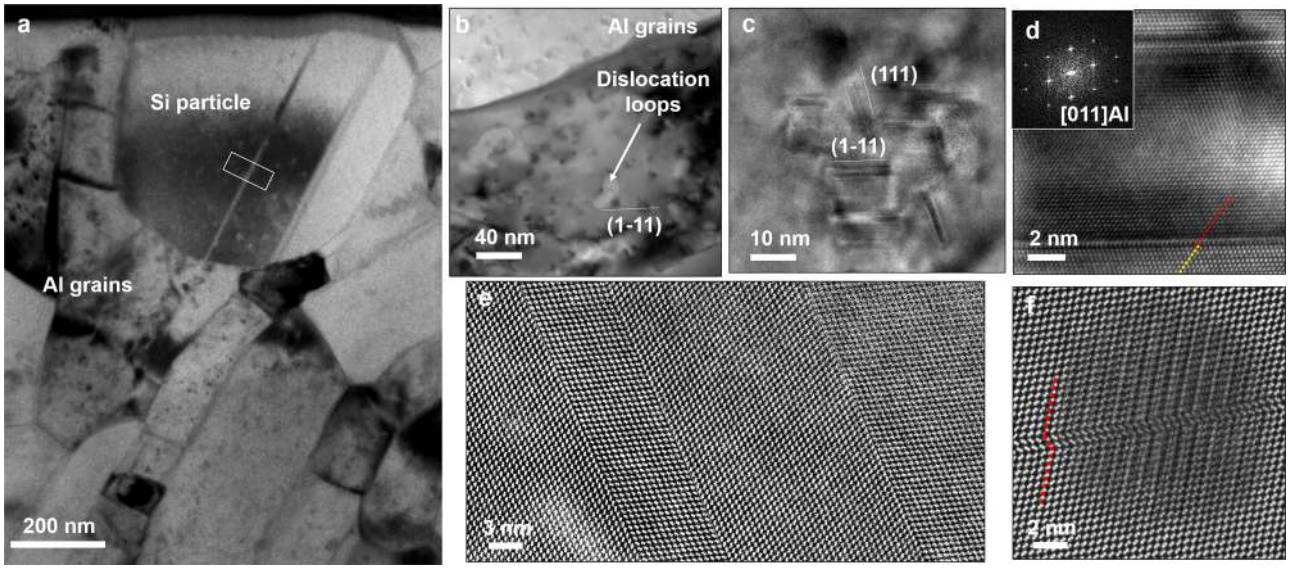

Fig. 4 Defect structures in sheared region. a BFTEM image of Al nanograins and a fragmented eutectic Si phase (marked). **b** BFTEM image showing the dislocation loops in the Al grains. **c** Stacking faults in Al grains within the dislocation loops. **d** phase contrast image showing the discontinuity, or the fault, in Al stacking. The inset is the FFT of the image depicting the [011] zone axis of Al. **e** High-magnification STEM-HAADF image of the deformation twins in the fragmented eutectic Si. **f** STEM-HAADF image of the atomic columns of the fragmented eutectic Si depicting nanotwin shearing across the Al nanoprecipitate.

were completely healed after shear deformation. Healing of nanovoids can be related to friction nano-welding, stress relaxation after processing, or the local heating due to friction. However, the degree to which this effect is observed can vary with the location of examination; hence, further investigation is required to fully elucidate the mechanisms behind this phenomenon.

Microstructure-based finite element modeling was conducted to further simulate the stress and plastic strain accumulation at an early stage of cyclic deformation that can drive the type of microstructural evolution observed in the Al–4Si alloys examined in this study. An SEM-BSE image of a 200×200 µm representative area of the Al–4Si alloy (Fig. 5a) was discretized into finite elements using the open-source code OOF2[48], as shown in Fig. 5b. The two-phase representative volume element (RVE) mesh was then imported into the ABAQUS standard commercial finite element code. Material properties were assigned to each phase: for Al, Young's modulus $E = 70$ GPa, Poisson's ratio $\nu = 0.33$, yield stress $\sigma_y = 117$ MPa, ultimate stress $\sigma_u = 200$ MPa, and ultimate strain $\varepsilon_u = 0.28$; for Si, $E = 130$ GPa, $\nu = 0.27$, $\sigma_y = 200$ MPa, $\sigma_u = 300$ MPa, and $\varepsilon_u = 0.05$. Plane strain elements (CPE3) were used in the model.

To simulate reciprocal shear deformation on the RVE domain, three loading cycles were considered using the loading pattern given in Fig. 5c. All the nodes on the RVE bottom boundary ($y = 0$) were fixed in both the x and y directions, while cyclic shear displacements were applied in the x direction at all the nodes along the top of the RVE domain. In addition, periodic boundary conditions were applied to the RVE domain, in which the nodes on the left and right boundaries were required to have the same displacements in the x direction. Figure 5d shows the von Mises stress distribution on the RVE after three loading cycles. Higher stress is predicted in the Si precipitates and along the grain boundaries in comparison to the Al matrix. The continued accumulation of von Mises stress can lead to eventual fragmentation of Si precipitates. The model predicted equivalent plastic strain contours after three loading cycles, which are presented in Fig. 5e. This plastic strain accumulation in the microstructure presumably drives dynamic recrystallization and the substantial microstructural refinement that improves the mechanical properties of the Al–4Si alloy.

In summary, we have demonstrated that shear deformation can be effective at modifying the microstructural hierarchy and defect structures in a binary Al–4Si alloy. A high degree of grain refinement in the Al matrix, from an initial grain size of ~500 µm to a ~100 nm final grain size, resulted from the reciprocating shear deformation. The eutectic Si phase was fragmented and redistributed in the shear-deformed microstructure in the form of (1) a 0.5–1 µm fragmented, deformed eutectic Si phase with ~95 at.% Si; (2) a nanoscale Si-rich phase along the Al grain boundaries with ~75 at.% Si; and (3) an heterogenous nanoscale clustering of Si within the Al matrix. The average dissolved Si concentration in the ultrafine Al matrix grains after deformation was 0.30 at.%. Both the Al matrix and Si phases displayed increased intermixing as a result of shear deformation. Dislocation Frank loops and stacking faults were observed in the Al matrix after deformation, and an abundance of nanotwins and stacking faults were found in the fragmented Si phase. Additionally, we demonstrated that the multiscale, microstructural hierarchy induced by shear deformation can further strengthen the alloy, in combination with the Hall–Petch strengthening by grain refinement. Micropillar compression tests indicated a twofold increase in the flow stresses due to shear-induced microstructural changes in of the alloy. A more detailed analysis of the deformation mechanisms activated in the highly refined shear-deformed alloy is currently ongoing and will be the subject of a future publication. The microstructural refinement and enhancement in mechanical properties observed in our study are analogous to observations from Al–Si alloys processed using FSP[1,3–6,36,49]. These results highlight the promise of using controlled shear deformation during SPP as a versatile approach to engineer hierarchical microstructures in alloys to achieve superior mechanical properties.

Methods

The binary hypoeutectic Al-4 at.% Si alloy (to be noted as Al–4Si through the remainder of the paper) was cast and remelted five times for homogenization. Samples with dimensions of $20 \times 10 \times 3$ mm were cut using a slow speed saw, mechanically ground to 2000 grit, and metallographically polished using a 0.02 µm colloidal silica solution. The microstructure of the as-cast alloy was characterized using scanning electron microscopy (SEM) backscattered electron imaging. The as-cast alloys were subjected to shear deformation in dry air at room temperature

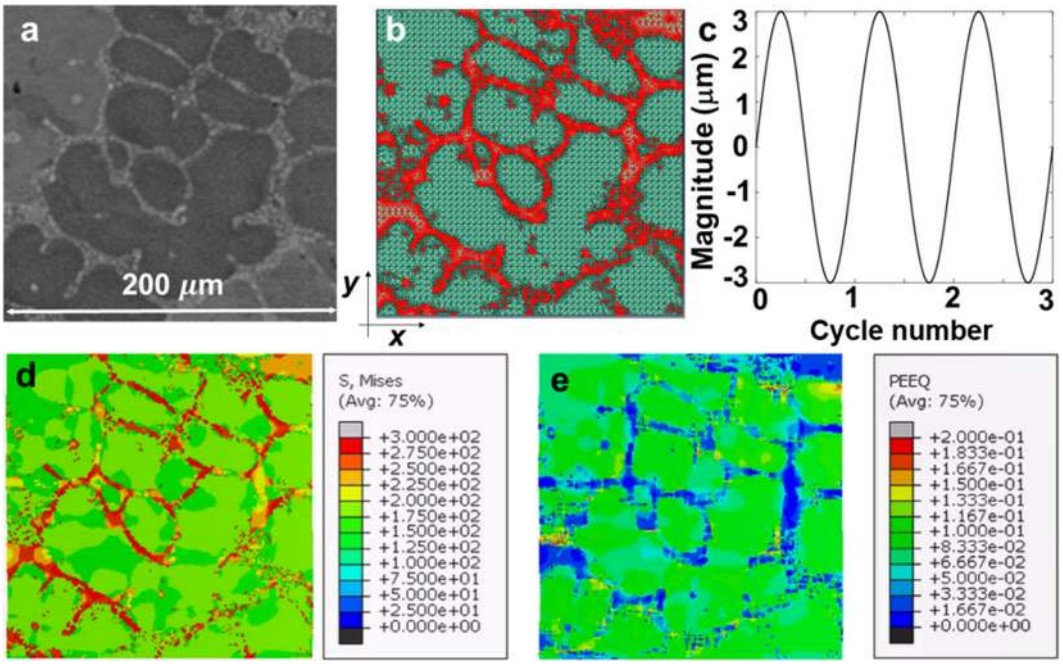

Fig. 5 Microstructure-based finite element modeling. **a** 200 × 200 μm^2 SEM-BSE image of an Al–4Si alloy and its representation as a computational representative volume element; **b** Si (red) and Al (green) occupying 18% and 82% of the mesh area, respectively; **c** the simulated loading cycle illustrates reciprocating shear deformation; **d** von Mises stress contours; and **e** accumulated equivalent plastic strain distribution from the 2-D, microstructure-based finite element shear model.

using an Anton Paar pin-on-disk tribometer. A 6 mm diameter stainless-steel sphere with a load of 1 N and linear speed of 200 mm/s was used in reciprocating mode for 5000 cycles, with a stroke length of 14 mm. The microstructures of the undeformed and shear-deformed regions were characterized using SEM, transmission and scanning transmission electron microscopy (TEM and STEM), and atom probe tomography (APT). The SEM imaging and sample preparation for S/TEM and APT (using the focused-ion beam (FIB) lift-out technique) was performed using a Thermo Fisher Scientific Quanta 200 FIB-SEM outfitted with an Oxford Instruments X-ray EDS system for compositional analysis. An FEI Titan 80–300 operated at 300 kV and an aberration, probe corrected, JEOL ARM200F operated at 200 kV were used for S/TEM. A CAMECA LEAP 4000X HR APT was used in pulsed voltage mode at a 200 KHz pulse frequency with 20% pulse fraction, a specimen temperature of 50–60 K, and a detection rate that was maintained at 0.005 atoms/pulse.

To compare the local deformation behavior of the as-cast to the sheared microstructures, micropillars were fabricated from both regions using FIB micromachining (FEI Scios) and tested under compression (using an Alemnis SEM indenter system. A FIB workstation (Tescan Vela) was used for milling the micropillars using a three-step process. First, stepped circles with an outer radius of 20 μm and inner radius of 5 μm were milled using an accelerating voltage of 30 kV and a current of 6 nA, stopping when the crater floor first reached the interface between the film and the substrate. Second, an annulus was milled at 30 kV and 1.6 nA to reduce the pillar diameter and sidewall taper. Finally, a polishing circle was used under the same milling conditions as in the previous step to achieve the final pillar diameter. The diameter was selected to be 40% of the film thickness, resulting in pillars with a nominal aspect ratio of 2.5.

Detailed microstructural analysis and the mechanical property assessment were conducted on the region directly below the center of the wear track (highlighted in Fig. 2b). A 2-D, microstructure-based finite element reciprocating shear deformation model[50,51] was also employed to analyze stress and plastic strain accumulation in the microstructure and to simulate the von Mises stress distribution and equivalent plastic strain after three cycles of reciprocal shear deformation.

Data availability

The data that support results of the presented study are available from the corresponding author upon reasonable request.

Received: 22 May 2020; Accepted: 30 September 2020;
Published online: 12 November 2020

References

1. Ma, Z., Sharma, S. R., Mishra, R. S. & Mahoney, M. W. Microstructural modification of cast aluminum alloys via friction stir processing. In *Materials Science Forum* (eds. Candra, T., Torralba, J. M. & Sakai, T.) (Transtec Publications, 1999, 2003).
2. Whalen, S. et al. High ductility aluminum alloy made from powder by friction extrusion. *Materialia* **6**, 100260 (2019).
3. Saini, N., Dwivedi, D., Jain, P. & Singh, H. Surface modification of cast Al-17% Si alloys using friction stir processing. *Procedia Eng.* **100**, 1522–1531 (2015).
4. Ma, Z. Y., Sharma, S. R. & Mishra, R. S. Microstructural modification of as-cast Al-Si-Mg alloy by friction stir processing. *Metall. Mater. Trans. A* **37a**, 3323–3336 (2006).
5. Jana, S., Mishra, R. S., Baumann, J. A. & Grant, G. J. Effect of friction stir processing on microstructure and tensile properties of an investment cast Al-7Si-0.6 Mg alloy. *Metall. Mater. Trans. A* **41**, 2507–2521 (2010).
6. Nelaturu, P., Jana, S., Mishra, R. S., Grant, G. & Carlson, B. E. Influence of friction stir processing on the room temperature fatigue cracking mechanisms of A356 aluminum alloy. *Mater. Sci. Eng. A* **716**, 165–178 (2018).
7. Pouryazdan, M., Kaus, B. J. P., Rack, A., Ershov, A. & Hahn, H. Mixing instabilities during shearing of metals. *Nat. Commun.* **8**, 1611 (2017).
8. Haug, C. et al. Early deformation mechanisms in the shear affected region underneath a copper sliding contact. *Nat. Commun.* **11**, 839 (2020).
9. Greiner, C., Gagel, J. & Gumbsch, P. Solids under extreme shear: friction-mediated subsurface structural transformations. *Adv. Mater.* **31**, 1806705 (2019).
10. Laube, S. et al. Solid solution strengthening and deformation behavior of single-phase Cu-base alloys under tribological load. *Acta Mater.* **185**, 300–308 (2020).
11. Wang, M., Averback, R. S., Bellon, P. & Dillon, S. Chemical mixing and self-organization of Nb precipitates in Cu during severe plastic deformation. *Acta Mater.* **62**, 276–285 (2014).
12. Vo, N. Q. et al. Atomic mixing in metals under shear deformation. *JOM* **65**, 382–389 (2013).
13. R, M., Bellon, P. & Averback, R. S. Wear resistance of Cu/Ag multilayers: a microscopic study. *ACS Appl. Mater. Interfaces* **10**, 15288–15297 (2018).
14. Chu, K. et al. Sliding wear induced subsurface microstructural evolution in nanocrystalline Nb-Ag binary alloys and its impact on tribological performance. *Wear* **392-393**, 69–76 (2017).
15. Ashkenazy, Y., Pant, N., Zhou, J., Bellon, P. & Averback, R. S. Phase evolution of highly immiscible alloys under shear deformation: Kinetic pathways, steady states, and the lever-rule. *Acta Mater.* **139**, 205–214 (2017).

16. Ren, F., Bellon, P. & Averback, R. S. Nanoscale self-organization reaction in Cu–Ag alloys subjected to dry sliding and its impact on wear resistance. *Tribol. Int.* **100**, 420–429 (2016).
17. Odunuga, S., Li, Y., Krasnochtchekov, P., Bellon, P. & Averback, R. S. Forced chemical mixing in alloys driven by plastic deformation. *Phys. Rev. Lett.* **95**, 045901–045905 (2005).
18. Cai, W. & Bellon, P. Subsurface microstructure evolution and deformation mechanism of Ag–Cu eutectic alloy after dry sliding wear. *Wear* **303**, 602–610 (2013).
19. An, X. et al. Atomic-scale investigation of interface-facilitated deformation twinning in severely deformed Ag-Cu nanolamellar composites. *Appl. Phys. Lett.* **107**, 011901 (2015).
20. Ren, F. et al. Sliding wear-induced chemical nanolayering in Cu–Ag, and its implications for high wear resistance. *Acta Mater.* **72**, 148–158 (2014).
21. Sarkar, A. D. & Clarke, J. Friction and wear of aluminium-silicon alloys. *Wear* **61**, 157–167 (1980).
22. Din, T. & Campbell, J. High strength aerospace aluminium casting alloys: a comparative study. *Materi. Sci. Technol.* **12**, 644–650 (1996).
23. Apelian, D. *Aluminum Cast Alloys: Enabling Tools for Improved Performance* 6–17 (North American Die Casting Association, 2009).
24. Shabestari, S. & Shahri, F. Influence of modification, solidification conditions and heat treatment on the microstructure and mechanical properties of A356 aluminum alloy. *J. Mater. Sci.* **39**, 2023–2032 (2004).
25. Yu, Y., Song, P., Kim, S. & Lee, J. Possibility of improving tensile strength of semi-solid processed A356 alloy by a post heat treatment at an extremely high temperature. *Scr. Mater.* **7**, 767–771 (1999).
26. Mayer, H., Papakyriacou, M., Zettl, B. & Stanzl-Tschegg, S. Influence of porosity on the fatigue limit of die cast magnesium and aluminium alloys. *Int. J. Fatigue* **25**, 245–256 (2003).
27. Zeren, M. The effect of heat-treatment on aluminum-based piston alloys. *Materi. Des.* **28**, 2511–2517 (2007).
28. Davidson, C., Griffiths, J. & Machin, A. The effect of solution heat-treatment time on the fatigue properties of an Al-Si-Mg casting alloy. *Fatigue Fract. Eng. Mater. Struct.* **25**, 223–230 (2002).
29. Sjölander, E. & Seifeddine, S. The heat treatment of Al–Si–Cu–Mg casting alloys. *J. Mater. Process. Technol.* **210**, 1249–1259 (2010).
30. Kashyap, K., Murali, S., Raman, K. & Murthy, K. Casting and heat treatment variables of Al–7Si–Mg alloy. *Mater. Sci. Technol.* **9**, 189–204 (1993).
31. Ogris, E., Wahlen, A., Lüchinger, H. & Uggowitzer, P. J. On the silicon spheroidization in Al–Si alloys. *J. Light Metals* **2**, 263–269 (2002).
32. Hurley, T. J. & Atkinson, R. J. Effects of modification practice on aluminum A356 alloys. *AFS Transactions* **93**, 291–296 (1985).
33. Barrirero, J. et al. Cluster formation at the Si/liquid interface in Sr and Na modified Al–Si alloys. *Scr. Mater.* **117**, 16–19 (2016).
34. Barrirero, J. et al. Comparison of segregations formed in unmodified and Sr-modified Al–Si alloys studied by atom probe tomography and transmission electron microscopy. *J. Alloys Compd.* **611**, 410–421 (2014).
35. Kang, H. S. et al. Effective parameter for the selection of modifying agent for Al-Si alloy. *Mat. Sci. Eng. A* **449**, 334–337 (2007).
36. Ma, Z., Sharma, S. & Mishra, R. Effect of friction stir processing on the microstructure of cast A356 aluminum. *Mater. Sci. Eng. A* **433**, 269–278 (2006).
37. Hurley, T. & Atkinson, R. Effects of modification practice on aluminum A356 alloys. *AFS Trans.* **93**, 291–296 (1985).
38. Qiyang, L., Qingchun, L. & Qifu, L. Modification of Al· Si alloys with sodium. *Acta Metall. Mater.* **39**, 2497–2502 (1991).
39. Frøseth, A. G., Holmestad, R., Derlet, P. M. & Marthinsen, K. Improved tight-binding parametrization for the simulation of stacking faults in aluminum. *Phys. Rev. B* **68**, 012105 (2003).
40. Barrirero, J. et al. Comparison of segregations formed in unmodified and Sr-modified Al–Si alloys studied by atom probe tomography and transmission electron microscopy. *J. Alloys Compd.* **611**, 410–421 (2014).
41. Stoyanov, P., Linsler, D., Schlarb, T., Scherge, M. & Schwaiger, R. Dependence of tribofilm characteristics on the running-in behavior of aluminum–silicon alloys. *J. Mater. Sci.* **50**, 5524–5532 (2015).
42. Armstrong, R. W. Hall–Petch relationship: use in characterizing properties of aluminum and aluminum alloys. In *Encyclopedia of Aluminum and it Alloys* (eds. Totton, G. E. & Tiryakioglu, M.) 1–30 (Department of Mechanical Engineering University of Maryland College Park, 2016).
43. Dieter, G. E. & Bacon, D. J. *Mechanical Metallurgy* (McGraw-hill, New York, NY, 1986).
44. Schulthess, T., Turchi, P., Gonis, A. & Nieh, T.-G. Systematic study of stacking fault energies of random Al-based alloys. *Acta Mater.* **46**, 2215–2221 (1998).
45. An, X., Wu, S., Wang, Z. & Zhang, Z. Significance of stacking fault energy in bulk nanostructured materials: insights from Cu and its binary alloys as model systems. *Prog. Mater. Sci.* **101**, 1–45 (2019).
46. Wu, X. L., Li, B. & Ma, E. Vacancy clusters in ultrafine grained Al by severe plastic deformation. *Appl. Phys. Lett.* **91**, 141908–141921 (2007).
47. Rohatgi, A., Vecchio, K. S. & Gray, G. T. The influence of stacking fault energy on the mechanical behavior of Cu and Cu-Al alloys: deformation twinning, work hardening, and dynamic recovery. *Metall. Mater. Trans. A* **32**, 135–145 (2001).
48. Langer, S., García, R. E. & Reid, A. *OOF2* https://nanohub.org/resources/oof2 (2007).
49. Kumar, N. & Mishra, R. Thermal stability of friction stir processed ultrafine grained AlMgSc alloy. *Mater. Charact.* **74**, 1–10 (2012).
50. Sun, X., Choi, K. S., Soulami, A., Liu, W. N. & Khaleel, M. A. On key factors influencing ductile fractures of dual phase (DP) steels. *Mater. Sci. Eng. A* **526**, 140–149 (2009).
51. Soulami, A. et al. Predicting fracture toughness of TRIP 800 using phase properties characterized by in-situ high-energy x-ray diffraction. *Metall. Mater. Trans. A* **41**, 1261–1268 (2010).

Acknowledgements

This work was supported by the Laboratory Directed Research and Development program at Pacific Northwest National Laboratory (PNNL) as part of the Solid Phase Processing Science initiative. A portion of this research was performed using facilities at the Environmental Molecular Sciences Laboratory, a national scientific user facility sponsored by the U.S. Department of Energy's (DOE's) Office of Biological and Environmental Research and located at PNNL. PNNL is a multiprogram national laboratory operated by Battelle for the DOE under Contract DEAC05-76RL01830. S.P. and S.V. acknowledge funding from NSF MRI #1726897 and DOE DE-NE0008739 for this work.

Author contributions

B.G. conducted the experiments including tribometry, sample preparation using FIB, experimental examination by TEM and APT; M.O. helping in the HRTEM imaging; S.V. performed the nanomechanical testing under the guidance of S.P.; L.L. performed the FEI-based simulation guided by A.S.; E.K. helped in APT sample preparation; A.R., P.V.S., C.A.P., and S.M. participated in scientific discussion helping in conceptualizing and refining the work; A.D. directed the research, conceptualized the idea, and provided scientific guidance. B.G. and A.D. wrote the first draft of the manuscript and all the authors contributed in revising it.

Competing interests

The authors declare no competing interests.

Additional information

Supplementary information is available for this paper at https://doi.org/10.1038/s43246-020-00087-x.

Correspondence and requests for materials should be addressed to A.D.

Peer review information Primary handling editors: Xiaoyan Li, John Plummer

Reprints and permission information is available at http://www.nature.com/reprints

Publisher's note Springer Nature remains neutral with regard to jurisdictional claims in published maps and institutional affiliations.

Open Access This article is licensed under a Creative Commons Attribution 4.0 International License, which permits use, sharing, adaptation, distribution and reproduction in any medium or format, as long as you give appropriate credit to the original author(s) and the source, provide a link to the Creative Commons license, and indicate if changes were made. The images or other third party material in this article are included in the article's Creative Commons license, unless indicated otherwise in a credit line to the material. If material is not included in the article's Creative Commons license and your intended use is not permitted by statutory regulation or exceeds the permitted use, you will need to obtain permission directly from the copyright holder. To view a copy of this license, visit http://creativecommons.org/licenses/by/4.0/.

© The Author(s) 2020